Bulletin of the Seismological Society of America, Vol. 101, No. 5, pp. 2296–2307, October 2011, doi: 10.1785/0120100075

# Earthquake Ruptures with Strongly Rate-Weakening Friction and Off-Fault Plasticity, Part 1: Planar Faults

by Eric M. Dunham, David Belanger, Lin Cong, and Jeremy E. Kozdon

Abstract We study dynamic rupture propagation on flat faults using 2D plane strain models featuring strongly rate-weakening fault friction (in a rate-and-state framework) and off-fault Drucker–Prager viscoplasticity. Plastic deformation bounds stresses near the rupture front and limits slip velocities to ~10 m/s, a bound expected to be independent of earthquake magnitude. As originally shown for ruptures in an elastic medium (Zheng and Rice, 1998), a consequence of strongly rate-weakening friction is the existence of a critical background stress level at which self-sustaining rupture propagation, in the form of self-healing slip pulses, is just barely possible. At higher background stress levels, ruptures are cracklike. This phenomenology remains unchanged when allowing for off-fault plasticity, but the critical stress level is increased. The increase depends on the extent and magnitude of plastic deformation, which is influenced by the orientation of the initial stress field and the proximity of the initial stress state to the yield surface.

## Introduction

As recent laboratory experiments have shown, the frictional resistance to slip decreases dramatically at coseismic slip rates (Tsutsumi and Shimamoto, 1997; Tullis and Goldsby, 2003a, 2003b; Prakash and Yuan, 2004; Di Toro *et al.*, 2004; Hirose and Shimamoto, 2005; Beeler *et al.*, 2008). This is referred to as dynamic weakening. One consequence of strongly rate-weakening friction laws is that for a range of initial stress conditions, ruptures occur as self-healing slip pulses instead of as cracks (Cochard and Madariaga, 1994, 1996; Beeler and Tullis, 1996; Zheng and Rice, 1998; Lapusta and Rice, 2003; Noda *et al.*, 2009). The same phenomenology applies when other dynamic weakening mechanisms, such as thermal pressurization of pore fluids, act in concert with strongly rate-weakening friction laws (Noda *et al.*, 2009).

For uniform prestress conditions, the rupture mode is primarily determined by the background shear stress on the fault, $\tau^b$. According to the understressing theory of Zheng and Rice (1998) for ruptures in elastic solids, there exists a critical background stress level, $\tau^{\text{pulse}}$, below which ruptures cannot take the form of cracks. No conclusive statement can be made about rupture mode for $\tau^b > \tau^{\text{pulse}}$, but it is seen in numerical experiments that self-sustaining slip pulses occur within a narrow range of $\tau^b$ around $\tau^{\text{pulse}}$ (Zheng and Rice, 1998; Noda *et al.*, 2009). The range is generally around 10% of $\tau^{\text{pulse}}$ for the friction law used in this work; a more complete theory that helps to quantify the occurrence of pulses is given by Zheng and Rice (1998). This phenomenology is also observed for shear ruptures in the laboratory (Lykotrafitis *et al.*, 2006). It is expected that natural faults are most likely to host ruptures soon after stresses on the fault first reach the minimum level that permits propagation, provided that nucleation events are sufficiently frequent.

Several lines of reasoning suggest that natural earthquakes occur in the self-healing rupture mode. Seismic inversions show that the duration of slip at a particular point on the fault is much shorter than expected from cracklike models (Heaton, 1990). In their simulations of ruptures with laboratory-based friction law parameters, Noda *et al.* (2009) have also found that only pulselike ruptures exhibit the observed scaling between slip and rupture length. Cracklike ruptures produce about an order of magnitude too much of slip for a given rupture length.

Additional evidence supporting dynamic weakening of natural faults comes from measurements of stress levels and heat flow around major faults. For laboratory-based parameters, the critical stress level separating pulses and cracks in an elastic medium is ~0.2–0.3 times the effective normal stress, far less than initial stress levels that are conventionally assumed in rupture modeling (e.g., Harris *et al.*, 2009). Furthermore, almost all slip occurs at even lower stress levels than the already low $\tau^b$, thus minimizing the production of heat during frictional sliding. Dynamic weakening thus offers a possible explanation for the lack of measurable heat flow anomalies around the San Andreas fault (Brune *et al.*, 1969; Lachenbruch and Sass, 1980; Saffer *et al.*, 2003) and is consistent with direct measurements and inferences of the stress state surrounding the San Andreas fault (Zoback *et al.*, 1987; Hardebeck and Michael, 2004; Hickman and Zoback,

2004). A more detailed discussion of these issues is given by Noda *et al.* (2009).

Existing theory and models dealing with strongly rate-weakening friction laws have thus far been restricted to ruptures in an elastic medium. But those models predict extreme stress conditions and unreasonably high slip velocities near the rupture front. For example, the simulations by Noda *et al.* (2009) predict peak slip velocities exceeding 100 m/s and fault-parallel strains of order 0.1. Prior to these conditions being reached, the material surrounding the fault will begin to deform inelastically with associated dissipation of energy.

The occurrence of inelastic deformation is expected on the basis of fault zone structure. The central fault core, consisting of ultra-cataclasites that host the slip surface, is surrounded by a broader damage zone extending ~10–100 m from the core. Rocks within the damage zone exhibit fractures at a variety of scales ranging from microcracks to macroscopic secondary faults showing evidence of shear slip and/or opening. Whether damage zones are formed by the stress concentrations around propagating rupture fronts or are relicts of the long-term fault maturation process through linkage of joints and microcracks remains unresolved. Mitchell and Faulkner (2009) and references therein provide a thorough geological characterization of fault damage zones and discussion of these issues.

Regardless of how damage zones form, the fractures contained within them will be activated by sufficiently high stresses during dynamic rupture along the main fault. We account for the associated inelastic deformation using the framework of continuum plasticity, with appropriately chosen yield functions and flow rules (such as the Mohr–Coulomb or Drucker–Prager formulations) (e.g., Rudnicki and Rice, 1975; Jaeger *et al.*, 2007). Recently these have been used in earthquake models (Andrews, 2005; Ben-Zion and Shi, 2005; Duan and Day, 2008; Templeton and Rice, 2008; Viesca *et al.*, 2008; Ma and Beroza, 2008).

The purpose of this study is to investigate how rupture dynamics with strongly rate-weakening friction laws (but neglecting thermal pressurization), and in particular the understressing theory of Zheng and Rice (1998), generalizes when accounting for off-fault inelastic deformation. Furthermore, while in this study our focus is on rupture propagation on flat faults, we consider in a companion study (Dunham *et al.*, 2011) the influence of fault roughness. When modeling slip on nonplanar surfaces, it is essential to consider plasticity to bound the otherwise unreasonable stress perturbations that develop around bends in the fault profile. The present study thus provides the basic framework upon which the investigation of rough faults can be built.

## Model Description

We study rupture propagation using 2D plane strain models (Fig. 1). The fault surface is the plane $y = 0$, which obeys a strongly rate-weakening friction law encapsulated in a rate-and-state framework. We allow for inelastic deformation

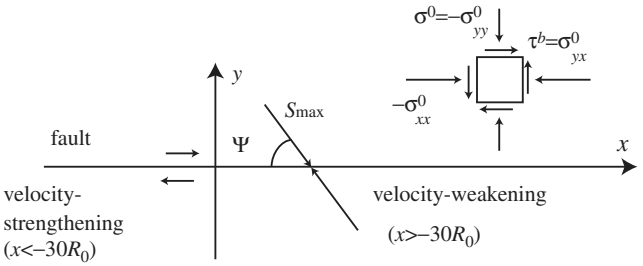


**Figure 1.** Plane strain model with right-lateral slip on a planar fault ($y = 0$). The medium is loaded with a spatially uniform stress state, with the direction of maximum compression inclined at the angle $\Psi$ to the fault.

of the material surrounding the fault using Drucker–Prager viscoplasticity. The medium is assumed to be homogeneous and infinite in extent, and is governed by momentum conservation,

$$\rho \frac{\partial v_i}{\partial t} = \frac{\partial \sigma_{ij}}{\partial x_j}, \tag{1}$$

for density $\rho$, particle velocity $v_i$, stress $\sigma_{ij}$, and the constitutive response,

$$\frac{\partial \sigma_{ij}}{\partial t} = L_{ijkl}(\dot{\epsilon}_{kl} - \dot{\epsilon}^p_{kl}). \tag{2}$$

$L_{ijkl}$ is the tensor of elastic moduli, $\dot{\epsilon}_{ij} = (1/2)(\partial v_i/\partial x_j + \partial v_j/\partial x_i)$ is the total strain rate, and $\dot{\epsilon}^p_{ij}$ is the plastic strain rate. The elastic strain rate is thus $\dot{\epsilon}_{kl} - \dot{\epsilon}^p_{kl}$, such that (2) is simply the time derivative of Hooke's law. Assuming isotropic elastic properties, $L_{ijkl}\dot{\epsilon}_{kl} = K\dot{\epsilon}_{kk}\delta_{ij} + 2G(\dot{\epsilon}_{ij} - \delta_{ij}\dot{\epsilon}_{kk}/3)$ for bulk modulus $K$ and shear modulus $G$. The $S$ wave speed is $c_s = \sqrt{G/\rho}$. We consider a Poisson solid, for which Poisson's ratio is $\nu = 1/4$, and the $P$ wave speed is $c_p = \sqrt{3}c_s$. The equations governing the evolution of plastic strain will be discussed shortly.

## Strongly Velocity-Weakening Fault Friction

The steady state friction coefficient used in this work features the extreme velocity-weakening response seen in recent experiments (Tsutsumi and Shimamoto, 1997; Tullis and Goldsby 2003a, 2003b; Prakash and Yuan, 2004; Di Toro *et al.*, 2004; Hirose and Shimamoto, 2005; Beeler *et al.*, 2008). The particular form we use is

$$f_{ss}(V) = f_w + \frac{f_{LV}(V) - f_w}{[1 + (V/V_w)^n]^{1/n}}, \tag{3}$$

with slip velocity $V$, weakening velocity $V_w$, fully weakened friction coefficient $f_w$, and a conventional low-velocity friction coefficient

$$f_{LV}(V) = f_0 - (b - a)\ln(V/V_0). \tag{4}$$

Here, $a$ is the direct-effect parameter, $b$ is the state-evolution parameter, and $f_0$ and $V_0$ are the reference friction coefficient and slip velocity, respectively. The form of equation (3) is such that $f_{ss}(V) \approx f_{LV}(V)$ for $V \ll V_w$ and $f_{ss}(V) \approx f_w$ for $V \gg V_w$. Laboratory experiments suggest that $V_w \sim 0.1$ m/s and $f_w \sim 0.2$. The abruptness of the transition between the two limits is controlled by the parameter $n$; the original flash-heating model (Rice, 1999; Beeler and Tullis, 2003; Rice, 2006; Beeler *et al.*, 2008) emerges in the $n \to \infty$ limit. Finite values of $n$ smooth the onset of strongly rate-weakening behavior. We prefer, for numerical accuracy, to have a smooth transition, so we choose $n = 8$ in this work.

Purely rate-weakening friction laws cannot be used because they can lead to mathematically ill-posed problems or unphysical phenomena (Rice *et al.*, 2001). Instead, we follow Noda *et al.* (2009) by encapsulating the steady state response (equation 3) in the experimentally motivated framework of rate-and-state friction in the slip law form (Rice, 1983):

$$f(V,\Theta) = a\text{arcsinh}\left(\frac{V}{2V_0}e^{\Theta/a}\right) \tag{5}$$

and

$$\frac{d\Theta}{dt} = -\frac{V}{L}[f(V,\Theta) - f_{ss}(V)], \tag{6}$$

in which $\Theta$ is the state variable. The fault strength $\tau$, which is always equal to the shear stress acting on the fault, is

$$\tau = f(V,\Theta)\sigma, \tag{7}$$

where $\sigma$ is the normal stress on the fault (taken to be positive in compression).

## Off-Fault Inelastic Response

The off-fault material is idealized as a Drucker–Prager elastic-plastic solid; we consider both rate-independent plasticity and viscoplasticity. The Drucker–Prager model, which is closely related to the Mohr–Coulomb model, describes inelastic deformation in brittle solids arising from frictional sliding of fractures and microcracks (Rudnicki and Rice, 1975; Templeton and Rice, 2008). The shear yield stress depends on the mean stress, with sensitivity determined by the internal friction coefficient of the material. It is also possible to include cohesion, but we neglect it in this study under the assumption that the material surrounding the fault has been highly damaged in previous events. The yield function is thus

$$F(\sigma_{ij}) = \bar{\tau} + \mu\sigma_{kk}/3, \tag{8}$$

in which $\bar{\tau} = \sqrt{s_{ij}s_{ij}/2}$ is the second invariant of the deviatoric stress tensor $s_{ij} = \sigma_{ij} - (\sigma_{kk}/3)\delta_{ij}$, $\sigma_{kk}/3$ is the mean stress, and $\mu$ is related to the internal friction coefficient. When $F(\sigma_{ij}) < 0$, the material response is elastic. See Figure 2a.

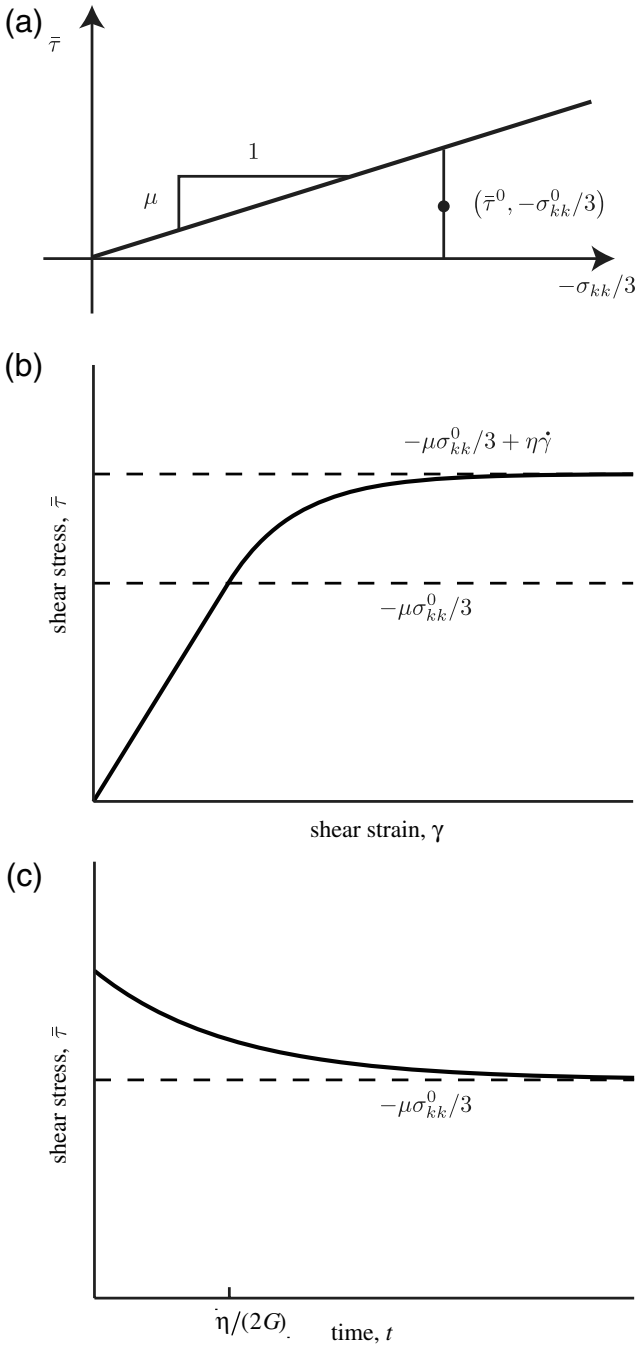


**Figure 2.** (a) Drucker–Prager yield condition with no cohesion. The initial stress state is marked with a filled circle. (b) Viscoplastic stress-strain history at a constant strain rate, $\dot{\gamma}$, for the case of pure shear deformation at constant mean stress. Response is linear elastic until stresses reach the yield stress, $-\mu\sigma^0_{kk}/3$. Stresses then exceed yield; asymptotically, the additional stress above yield is $\eta\dot{\gamma}$ for viscosity $\eta$. (c) Relaxation of stress to the yield surface, over a timescale $\sim\eta/G$ ($G$ is shear modulus), in the absence of additional strain.

We do not explicitly consider pore fluids in this study, though the stresses appearing in equations (7) and (8) should be the effective stresses if the medium is saturated with fluids. However, Viesca *et al.* (2008) have shown that the undrained

poroelastic response can be accounted for in exactly the framework we use, provided that certain parameters in the yield function and flow rule are modified appropriately.

A scalar measure of the shear plastic strain rate is the equivalent plastic strain rate, $\lambda$, which is defined as $\lambda = \sqrt{2\dot{e}^p_{ij}\dot{e}^p_{ij}}$ for deviatoric plastic strain rate $\dot{e}^p_{ij} = \dot{\epsilon}^p_{ij} - (\dot{\epsilon}^p_{kk}/3)\delta_{ij}$. The equivalent plastic strain, $\gamma^p$, is thus defined through $\lambda = d\gamma^p/dt$. During rate-independent plastic flow, $\lambda$ is determined such that stresses lie exactly on the yield surface, that is, $F(\sigma_{ij}) = 0$. Plastic flow is partitioned between the various components of the plastic strain rate tensor by the flow rule

$$\dot{\epsilon}^p_{ij} = \lambda P_{ij}(\sigma_{ij}), \tag{9}$$

with $P_{ij}(\sigma_{ij}) = s_{ij}/(2\bar{\tau}) + (\beta/3)\delta_{ij}$; $\beta$ determines the degree of plastic dilatancy, that is, the ratio of volumetric to shear plastic strain.

Under certain stress conditions, a material undergoing plastic deformation may become unstable to shear localization (Rudnicki and Rice, 1975). Localization is commonly observed in brittle materials loaded under compression. However, the rate-independent form of Drucker–Prager plasticity is known to be mathematically ill-posed if conditions permit localization, with the consequence that numerical solutions of these equations will not converge with mesh refinement. This is clearly illustrated in the context of dynamic rupture propagation by Templeton and Rice (2008). Andrews (2005) used a numerical viscoplastic-type regularization algorithm to obtain solutions free of localization. Others have simply employed the rate-independent form and acknowledged that localization in their numerical solutions was limited by the employed grid spacing (Duan and Day, 2008; Templeton and Rice, 2008; Viesca *et al.*, 2008).

In our work, we adopt a formulation of viscoplasticity that is known to be well-posed mathematically (Perzyna, 1966; Loret and Prevost, 1990; Sluys and de Borst, 1992). The formulation permits localization, but limits the localization process so that numerical solutions converge with mesh refinement. In this model, stresses are permitted to exceed the yield surface, and the additional stress above the yield surface (a scalar measure of which is $F(\sigma_{ij}) > 0$) obeys a viscous rheology. Stresses that exceed the yield condition relax back toward the yield surface in the absence of additional loading, and asymptotically flow at a stress level that increases with the applied strain rate. At a sufficiently high strain rate, the initial response is effectively elastic.

Mathematically, during plastic flow the yield condition $F(\sigma_{ij}) = 0$ is replaced with

$$\eta\lambda = F(\sigma_{ij}) \tag{10}$$

for viscosity $\eta$. Figure 2 illustrates properties of the viscoplastic response. The viscoplastic relaxation times we use in this work are chosen to be smaller than any other characteristic timescale in our problem, but large enough to be resolvable by the finite timestep used to integrate the discretized equations. Our choice of this rheology and the specific parameter values is motivated by the necessity of well-posedness for convergent numerical results. Efforts, such as those by Bhat *et al.* (2010), to formulate physically based constitutive laws that capture the rate dependence of inelastic deformation in brittle materials are needed.

Substituting the flow rule of equation (9) into Hooke's law in equation (2), and writing the resulting equation along with equation (10), gives the complete set of equations that determine the evolution of stress for a given strain rate history:

$$\frac{\partial\sigma_{ij}}{\partial t} = L_{ijkl}[\dot{\epsilon}_{kl} - \langle\lambda\rangle P_{kl}(\sigma_{ij})] \tag{11}$$

and

$$\eta\lambda = F(\sigma_{ij}), \tag{12}$$

where $\langle\lambda\rangle = \lambda$ for $\lambda > 0$ and zero otherwise (this formulation simply accounts for the lack of plastic flow when stresses are below yield).

The numerical method used to solve these equations is described in the Appendix.

## Initial Conditions and Model Parameters

We assume a spatially uniform prestress field, $\sigma^0_{ij}$. We fix $\sigma^0_{yy} = -\sigma^0$, the stress component responsible for the normal stress acting on a planar fault, and vary both $\sigma^0_{xy} = \tau^b$ and $\sigma^0_{xx}$. The latter is specified in terms of the angle, $\Psi$, between the maximum principal compressive stress and the fault surface $y = 0$, defined through the relation

$$\sigma^0_{xx} = \left[1 - \frac{2\sigma^0_{xy}}{\sigma^0_{yy}\tan(2\Psi)}\right]\sigma^0_{yy}, \tag{13}$$

(see Fig. 1). Following Templeton and Rice (2008), the initial out-of-plane normal stress is taken to be the average of the two in-plane normal stresses: $\sigma^0_{zz} = (\sigma^0_{xx} + \sigma^0_{yy})/2$. This stress component is only relevant during plastic flow and, for this particular choice, the Drucker–Prager yield function coincides with the Mohr–Coulomb condition (a correspondence that generally ceases once plastic flow ensues).

As given in Table 1, the material properties and initial stresses are representative of those at seismogenic depths, and parameters of the friction law (with the exception of state-evolution distance $L$) are similar to those used by Noda *et al.* (2009), who selected them from a compilation of laboratory data. The state-evolution distance, $L$, provides a slip scale that is used to nondimensionalize lengths and times as discussed shortly. For estimating hazard from large earthquakes, $L$ is typically regarded as a free parameter that is selected to model rupture propagation at a desired scale. With this in mind, we provide dimensionalized units

Table 1
Physical Properties and Model Parameters

| Parameter | | Symbol | Value |
|---|---|---|---|
| Material Properties | | | |
| | Shear modulus | $G$ | 32.04 GPa |
| | Shear wave speed | $c_s$ | 3.464 km/s |
| | Poisson's ratio | $\nu$ | 0.25 |
| | Drucker–Prager internal friction parameter | $\mu$ | $\sin[\arctan(0.7)] = 0.5735$ |
| | Drucker–Prager plastic dilatancy parameter | $\beta$ | $\mu/2 = 0.2867$ |
| | Drucker–Prager viscosity | $\eta$ | $0.1GR_0/c_s = 0.2775$ GPa · s |
| Friction-Law Parameters | | | |
| | Direct effect parameter | $a$ | 0.016 |
| | Evolution effect parameter | $b$ | 0.02 |
| | Reference slip velocity | $V_0$ | 1 $\mu$m/s |
| | Steady state friction coefficient at $V_0$ | $f_0$ | 0.7 |
| | State-evolution distance | $L$ | 0.2572 m |
| | Weakening slip velocity | $V_w$ | 0.17 m/s |
| | Fully weakened friction coefficient | $f_w$ | 0.13 |
| Initial Conditions | | | |
| | Normal stress on flat fault | $\sigma^0$ | 126 MPa |
| | Background shear stress | $\tau^b$ | variable |
| | Initial state variable | $\Theta(t=0)$ | 0.4367 |
| Other | | | |
| | Characteristic extent of state-evolution region | $R_0$ | 300 m |
| | Critical background shear stress | $\tau^{\text{pulse}}$ | $0.2429\sigma^0 = 30.6059$ MPa |

corresponding to faults of length ~100 km, though the requisite value of $L$ is far larger than that inferred from laboratory experiments.

For the steady state friction law (3) with our chosen parameters, the critical background stress $\tau^{\text{pulse}}$, as defined by Zheng and Rice (1998), is $\tau^{\text{pulse}} = 0.2429\sigma^0$ ($= 30.6059$ MPa for $\sigma^0 = 126$ MPa). The corresponding characteristic slip velocity during steady sliding, $V^{\text{pulse}}$, is that at the intersection of $f_{ss}(V)\sigma^0$ and the radiation-damping line just tangent to this curve: $V^{\text{pulse}} = 1.5474$ m/s.

While rate-and-state friction laws do not have well-defined peak and residual strengths, $\tau^p$ and $\tau^r$, we can estimate them as follows. At the rupture front, the shear stress is assumed to increase from the background value, $\tau^b$, to the peak strength, $\tau^p$, with negligible state evolution. The direct-effect response gives

$$\tau^p \approx \sigma^0[a\ln(V^p/V_0) + \Theta_{\text{ini}}] = \tau^b + a\sigma^0\ln(V^p/V_{\text{ini}}), \tag{14}$$

where $\Theta_{\text{ini}}$ and $V_{\text{ini}}$ are the initial state variable and initial slip velocity, respectively, and $V^p$ is the peak slip velocity at the rupture front. The residual strength is approximated as

$$\tau^r = f_{ss}(V^{\text{pulse}})\sigma^0, \tag{15}$$

giving $\tau^r = 0.1864\sigma^0$ ($= 23.4864$ MPa).

Next we relate $V^p$ to the strength drop, $\tau^p - \tau^r$, assuming a radiation-damping elastodynamic response:

$$V^p \approx 2c_s(\tau^p - \tau^r)/G. \tag{16}$$

We fix the static friction coefficient, $\tau^p/\sigma^0$, at 0.7 for all simulations by selecting $\Theta_{\text{ini}} = 0.4367$.

Assuming an exponential slip-weakening process at the rupture front (a fairly good approximation for the slip law), we can estimate the fracture energy as $\Gamma \approx (\tau^p - \tau^r)L$. By holding $\tau^p$ and $\tau^r$ fixed as we vary $\tau^b$, we also roughly preserve the spatial extent of the state-evolution region at the rupture front in the limit of vanishing rupture velocity, $R_0$, which we approximate using the formula (for Poisson's ratio of 1/4) given by Palmer and Rice (1973):

$$R_0 \approx \frac{3\pi}{4}\frac{G\Gamma}{(\tau^p - \tau^r)^2} \approx \frac{3\pi}{4}\frac{GL}{\tau^p - \tau^r}. \tag{17}$$

We nondimensionalize length and timescales using $R_0$ and $R_0/c_s$, respectively, but we also provide dimensional scales in our plots by choosing $L$ such that $R_0 = 300$ m. Particle and slip velocities are normalized by $c_s\Delta\tau/G$ and $2c_s\Delta\tau/G$, respectively, where $\Delta\tau = \tau^{\text{pulse}} - \tau^r$.

We use a uniform grid spacing $\Delta x = R_0/16$ (and in some cases $R_0/32$ or $R_0/64$ as part of refinement tests, see insets in Fig. 3). This prevents the contamination of our results by spurious oscillations. The computational domain, at the lowest resolution, is spanned by $4801 \times 2402$ grid points, and is terminated with absorbing boundary conditions (specifically, the amplitudes of the characteristic variables associated with waves entering the computational domain normal to the boundary are set to zero).

We use a nonzero $\eta$ in the viscoplastic rheology to ensure well-posed numerical simulations that converge with mesh refinement. The model, as defined, has two characteristic timescales: the viscoplastic relaxation time, $\eta/G$, and

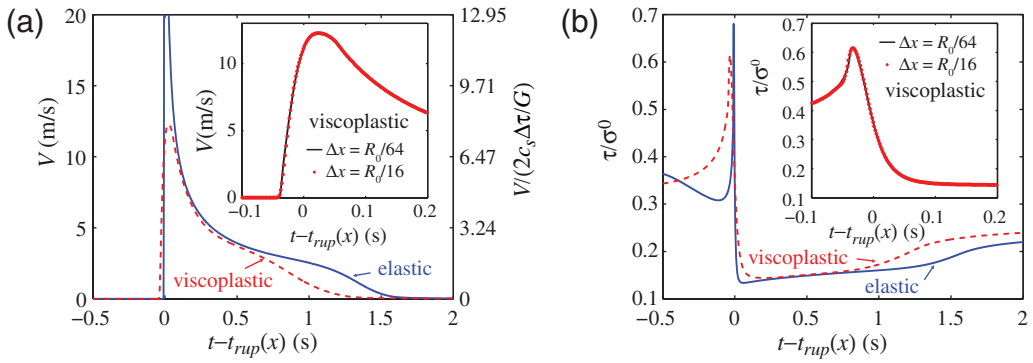


**Figure 3.** Time histories of (a) slip velocity and (b) shear stress for self-healing slip pulses in elastic and elastic-viscoplastic solids, at $x = 87.4R_0$ ($= 26.25$ km), for $\Psi = 50°$ and $\tau^b = 0.2857\sigma^0$. Time is relative to rupture front arrival time, $t_{\text{rup}}(x)$ (defined as the time at which slip first exceeds the state-evolution distance). Insets compare elastic-viscoplastic solutions at different levels of numerical resolution; the $L_2$ (root mean square) error of the solution with $\Delta x = R_0/16$ is about 1%. The color version of this figure is available only in the electronic edition.

the characteristic wave transit time across the state-evolution region, $R_0/c_s$. The latter also characterizes the timescale over which frictional weakening occurs at the rupture front. When the dimensionless ratio $\xi = (\eta/G)/(R_0/c_s) \ll 1$, then plasticity is important even during the rapid weakening process at the rupture front. Otherwise, the material response around the rupture front is effectively elastic. Except for a brief exploration of the role this parameter plays in rupture behavior, we use $\xi = 0.1$.

Ruptures are nucleated by instantaneously applying, at $t = 0$, a Gaussian-shaped shear stress perturbation on the fault centered at $x = 0$. The amplitude of the nucleating perturbation is $2\tau^{\text{pulse}}$; its width (the standard deviation of the Gaussian profile) is $R_0$. Ruptures are made unilateral by making the fault velocity-strengthening some distance to the left of the nucleation zone. Specifically, we increase $a$ linearly with distance from 0.016 to 0.024 in the region $-40R_0 < x < -20R_0$ and set $a = 0.024$ for $x < -40R_0$; $V_w$ is similarly increased by 5 m/s over the same region.

As $\tau^b$ is varied relative to $\tau^{\text{pulse}}$ in the simulations, we keep the static friction coefficient, $\tau^p/\sigma^0$, fixed at 0.7 by varying $V_{\text{ini}}$. The initial velocity field in the medium is piecewise constant (it is discontinuous across $y = 0$) and solely in the $x$ direction; that is, we set $v_x(t = 0) = \pm V_{\text{ini}}/2$ for the material above and below the fault, respectively, and $v_y(t = 0) = 0$. The initial slip velocity, together with the resolved shear and normal stress, is required to satisfy the friction law (7). That equation is solved for the initial value of the state variable.

## Ruptures on Flat Faults

In simulations of rupture propagation in linear elastic solids with strongly rate-weakening friction laws (e.g., Noda *et al.*, 2009), slip velocities can become extremely large (~300 m/s) at the rupture front; these are associated with fault-parallel strains of ~0.1 and unreasonably large fault-parallel stresses. The occurrence of off-fault plasticity limits these stresses, and peak slip velocities drop to ~10 m/s, consistent with the estimates of Sleep (2010). To the extent that our simulations indicate self-similar rupture growth, this bound is expected to be independent of earthquake magnitude. Figure 3 shows representative time histories of slip velocity and shear stress at a point on the fault for both elastic and elastic-viscoplastic off-fault response.

We next explore the role of the prestress orientation, $\Psi$, and background stress, $\tau^b$, on the distribution of plastic strain and rupture mode. As found by Templeton and Rice (2008) and Viesca *et al.* (2008) in their studies with slip-weakening friction, plastic strain accumulates almost instantaneously across a discontinuity surface emanating from the rupture front. This is also true for our models with strongly velocity-weakening rate-and-state friction, though the jump is smoothed by the finite viscoplastic relaxation time. Figure 4 confirms another conclusion of Templeton and Rice (2008) and Viesca *et al.* (2008): Unless $\Psi$ is quite low, plastic strain occurs on the extensional side of the fault (specifically, the side of the fault for which the direction of fault-parallel displacement is opposite to the propagation direction).

As $\tau^b$ is increased, self-sustaining ruptures are first seen for $\tau^b$ slightly larger than $\tau^{\text{pulse}}$; they take the form of slip pulses. At higher levels of $\tau^b$, the rupture mode is expected to switch to cracklike. This transition does occur, but is preceded by another form of slip pulse that is generated in response to arrest waves triggered by the forced termination of the rupture front propagating in the $-x$ direction as it enters the velocity-strengthening portion of the fault. This mechanism for generating pulselike ruptures is well known (Johnson, 1990). These rupture modes are illustrated in Figure 5.

We next quantify how the critical stress level required for rupture propagation is altered by plasticity. This is done by varying $\Psi$ and determining, for each $\Psi$, the minimum $\tau^b$ (to an accuracy of about 0.5 MPa) at which self-sustaining propagation is first observed. The results, presented in Figure 6, illustrate that the critical stress level increases with $\Psi$, particularly for $\Psi > 40°$. This can be understood as follows.

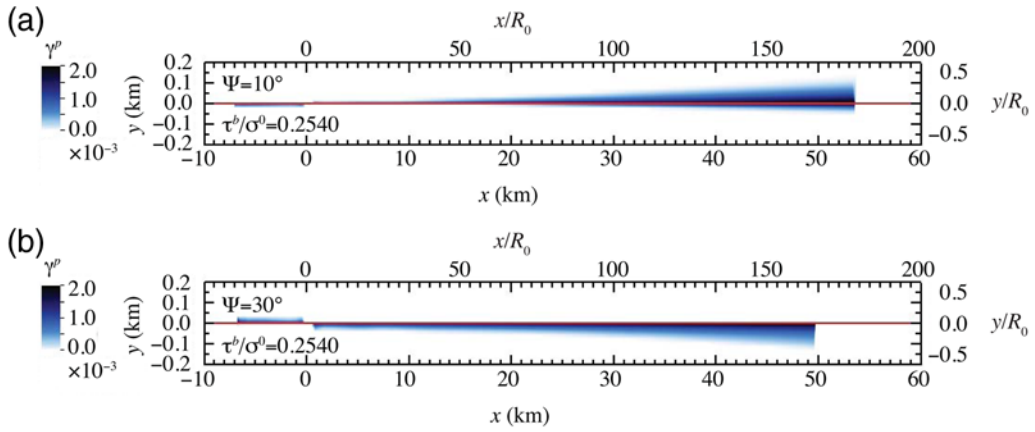


**Figure 4.** Distribution of plastic strain, $\gamma^p$, for (a) $\Psi = 10°$ and (b) $\Psi = 30°$, at time $t = 216.5R_0/c_s$ (= 18.75 s). Except for very small $\Psi$, plastic strain occurs exclusively in the extensional quadrants (slip is right-lateral). The extent of plastic strain increases for $\Psi > 30°$ (not shown). Plastic strain can be normalized by $\tau^p/2G = 1.38 \times 10^{-3}$. For both cases, the background stress, $\tau^b$, is slightly above that required for self-sustaining slip-pulse rupture propagation. Note factor of 20 exaggeration in $y$ direction. The color version of this figure is available only in the electronic edition.

Varying $\Psi$ alters the proximity of the prestress state to the yield surface. Following Templeton and Rice (2008), we quantify this as the closeness-to-failure ratio $\bar{\tau}^0/(-\mu\sigma^0_{kk})$, as illustrated graphically in Figure 2a. Figure 7a shows this ratio for $\sigma^0_{xy} = \tau^{\text{pulse}}$ as a function of $\Psi$. Similarly, prestress conditions in $(\bar{\tau}, -\sigma_{kk}/3)$-space are shown in Figure 7b for the two ruptures in Figure 4. For $\Psi$ below ≈5° or above ≈70°, the prestress state violates the yield condition; such prestress states cannot exist.

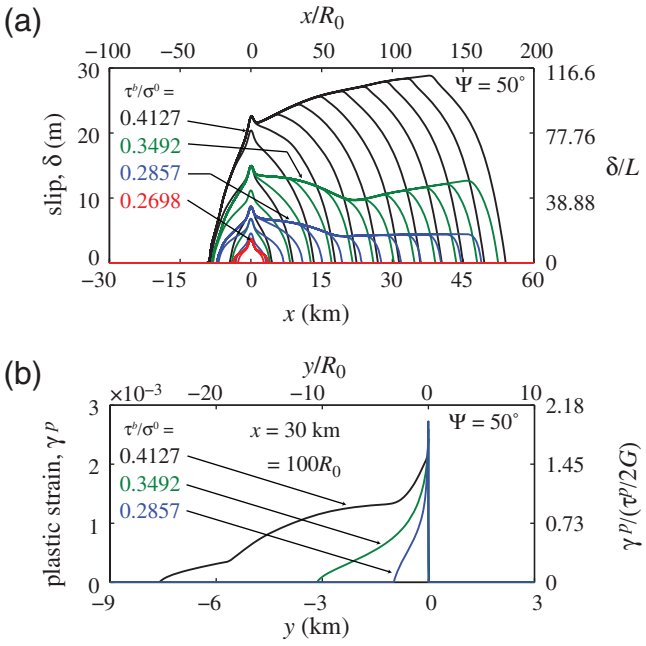


**Figure 5.** (a) Profiles of slip with time interval $17.32R_0/c_s$ (= 1.5 s) for $\Psi = 50°$, illustrating the transition in rupture mode as the background stress, $\tau^b$, is increased. Self-sustaining propagation is first possible around $\tau^b/\sigma^0 \approx 0.28$; for values slightly above this, ruptures take the form of self-healing slip pulses ($\tau^b/\sigma^0 = 0.2857$ and 0.3492 in figure). At higher $\tau^b/\sigma^0$, ruptures would be cracklike for uniform friction-law parameters, but arrest waves from the cessation of slip in the velocity-strengthening region ($x < -9$ km) cause pulselike ruptures ($\tau^b/\sigma^0 = 0.4127$ in figure). At even higher $\tau^b/\sigma^0$, ruptures become cracks (not shown). (b) Cross-sectional profile of plastic strain at $x = 100R_0$ (= 30 km); the spatial extent of plastic strain is roughly proportional to slip. The color version of this figure is available only in the electronic edition.

Numerical experiments indicate that as $\Psi$ approaches ≈70°, the extent of the region experiencing plastic strain increases greatly. This is because only slight stress perturbations (of the proper sign) are required to induce plastic flow. The associated increase of energy dissipation during plastic flow explains why $\tau^b$ must be substantially higher for self-sustaining rupture propagation at high values of $\Psi$, as seen in Figure 6.

By considering the prestress state alone, one might expect this effect to also occur for very low values of $\Psi$, but this is not seen. We can understand why by considering how stress in the vicinity of the rupture front evolves in $(\bar{\tau}, -\sigma_{kk}/3)$-space as the rupture passes. The stress is the

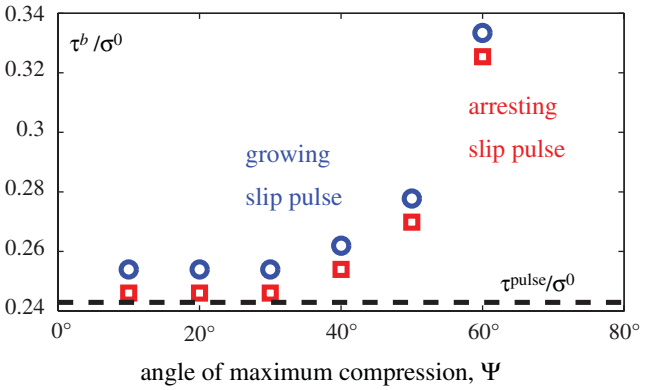


**Figure 6.** Minimum background stress, $\tau^b$, required for self-sustaining rupture propagation as a function of prestress orientation, $\Psi$. The color version of this figure is available only in the electronic edition.

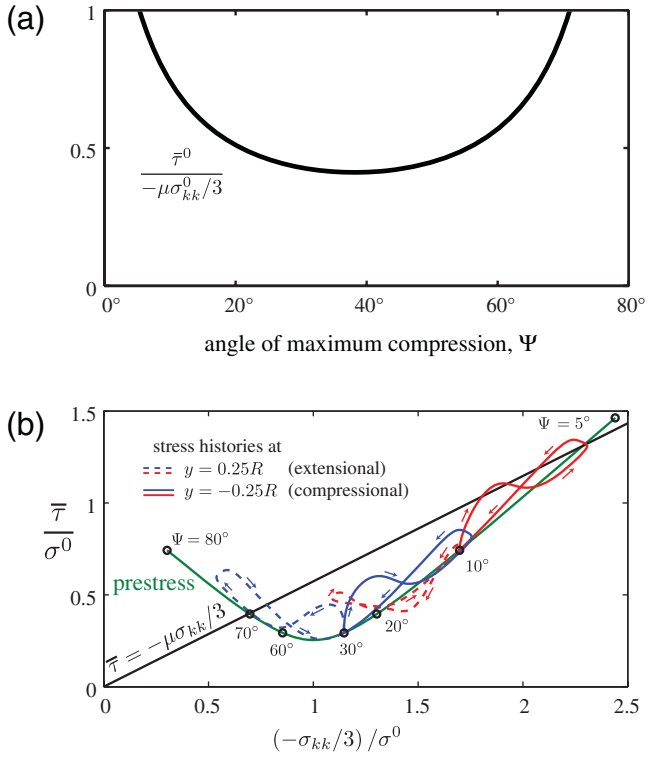


**Figure 7.** (a) Proximity of prestress state to yield surface, as defined by Templeton and Rice (2008); shown for $\sigma^0_{xy} = \tau^{\text{pulse}}$. Prestress states having Ψ less than ≈5° or greater than ≈70° violate the yield condition and are thus precluded. (b) Prestress and yield surface in $(\bar{\tau}, -\sigma_{kk}/3)$-space, for $\sigma^0_{xy} = 0.2540\sigma^0$ as in Figure 4. Also shown are predicted stress histories at points in extensional (dashed) and compressional (solid) quadrants using semi-infinite crack model of Poliakov *et al.* (2002) for Ψ = 10° and 30°. Arrows indicate direction of increasing time. Extent of strength drop region at rupture front is $R$; rupture velocity is $v_r = 0.85c_s$. The color version of this figure is available only in the electronic edition.

sum of the prestress and the stress perturbation due to slip: $\sigma_{ij} = \sigma^0_{ij} + \Delta\sigma_{ij}$. While $\sigma^0_{ij}$ depends on Ψ, we assume for purposes of comparison that $\Delta\sigma_{ij}$ does not. A simple model for $\Delta\sigma_{ij}$ is the nonsingular semi-infinite steady state crack model of Poliakov *et al.* (2002), which features a linear decrease in stress from $\tau^p$ to $\tau^r$ over a distance $R$. The off-fault response is linear elastic. We calculate the stress histories predicted by this model at points on either side of the fault. These are shown in Figure 7b for prestress states corresponding to the two ruptures shown in Figure 4. The histories are quite similar to those observed in the actual simulations.

For Ψ = 30°, a point on the extensional side of the rupture experiences increasing $\bar{\tau}$ and decreasing $-\sigma_{kk}/3$, both of which bring that point closer to the yield surface. On the compressional side of the fault, while $\bar{\tau}$ increases so does $-\sigma_{kk}/3$, and the yield condition is never reached. The stress histories are similar for larger values of Ψ. Plasticity is consequently limited to the extensional side of the rupture, consistent with Figure 4b.

In contrast, for Ψ = 10° a point on the compressional side of the rupture is driven to failure by a large increase in $\bar{\tau}$; the increase in $-\sigma_{kk}/3$ is insufficient to prevent plasticity. On the extensional side of the fault, the decrease in $-\sigma_{kk}/3$ is not accompanied by the increase in $\bar{\tau}$ that occurs for Ψ ≥ 30°, and the yield surface is not reached. Plasticity occurs on the compressional side of the fault for these very low values of Ψ, as seen in Figure 4a.

Decomposing the mean stress into the initial mean stress and a perturbation, $\sigma_{kk}/3 = \sigma^0_{kk}/3 + \Delta\sigma_{kk}/3$, we see that the perturbation to mean stress depends only on $\Delta\sigma_{ij}$ and is independent of the prestress. However, if we perform a similar decomposition for the deviatoric stress invariant, $\bar{\tau} = \bar{\tau}^0 + \Delta\bar{\tau}$, the nonlinearity of $\bar{\tau}$ (as defined following equation 8) introduces a dependence of $\Delta\bar{\tau}$ on Ψ. This explains why $\Delta\bar{\tau}$ is quite different for the two values of Ψ shown in Figure 7b, while $\Delta\sigma_{kk}/3$ is identical. Further discussions of stress fields near the tips of propagating ruptures are given by Poliakov *et al.* (2002) and Rice *et al.* (2005).

We close with a discussion of the influence of the viscoplastic relaxation time, $\eta/G$, relative to the wave transit time across the state-evolution region (which is also the state-evolution time), $R_0/c_s$, on rupture behavior. Figure 8 shows the distribution of plastic strain for several values of the dimensionless ratio $\xi = (\eta/G)/(R_0/c_s)$. We set $\beta = 0$ (no plastic dilatancy) in order to promote shear localization (Templeton and Rice, 2008). When $\xi \ll 1$, the off-fault response is effectively rate-independent, and shear localization features are observed that are sensitive to the numerical discretization employed (a manifestation of ill-posedness of the problem). For these specific parameters, the localization features are present for $\xi \leq 0.03$ but vanish abruptly for $\xi \geq 0.04$. When $\xi \gg 1$, the material response around the rupture front is effectively elastic, and both the rupture speed and peak slip velocity increase. The simulation results in this work (with the exception of those in Fig. 8) are for $\xi = 0.1$. Plasticity is thus important within the state-evolution region at the rupture front, but there are neither localization features nor issues with convergence of the numerical solution under mesh refinement.

## Conclusions

The occurrence of off-fault plasticity influences rupture dynamics on strongly rate-weakening faults in several ways. Stresses and slip velocities are bound to reasonable values at the rupture front, and there is an associated increase in the amount of energy dissipated during propagation. The location and extent of plastic strain is consistent with that found by Templeton and Rice (2008), in that it occurs almost exclusively on the extensional side of the fault except when the maximum principal compressive stress is inclined at a very shallow angle to the fault surface.

Strongly rate-weakening friction laws give rise to self-healing slip pulses in elastic solids for background stresses around a critical level (Zheng and Rice, 1998). We find that

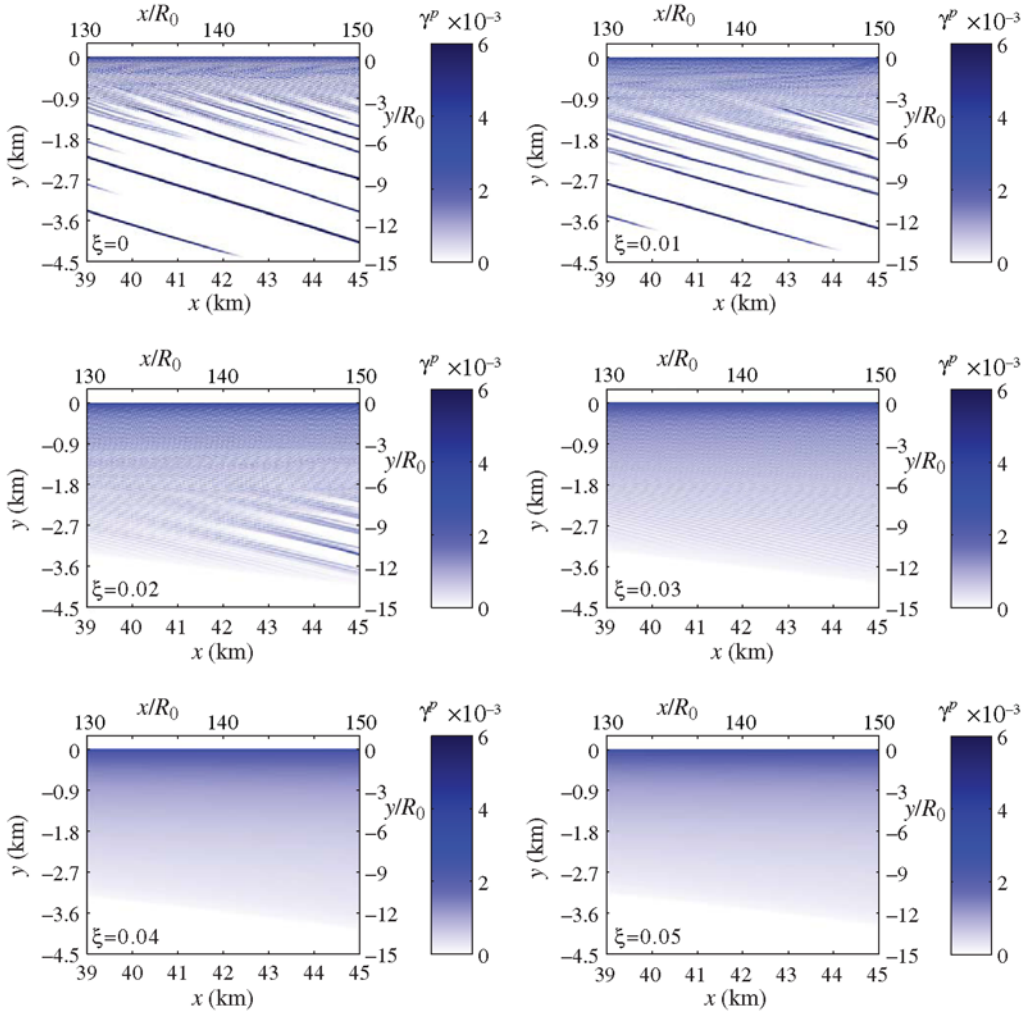


**Figure 8.** Influence of $\xi = (\eta/G)/(R_0/c_s)$, the ratio of the viscoplastic relaxation time to the duration of the strength drop at the rupture front, on plastic strain. As $\xi \to 0$ (the rate-independent plasticity limit), localization features appear and the solution becomes sensitive to the numerical discretization. The color version of this figure is available only in the electronic edition.

this remains the case when plasticity is taken into account, but the critical stress level is increased by plasticity. The magnitude of the increase depends strongly on the prestress orientation, in particular when the angle between the maximum compressive stress and the fault surface exceeds 40°–50°.

This study is the first of a two-part exploration of rupture dynamics on strongly rate-weakening faults with off-fault plasticity. The second part (Dunham *et al.*, 2011) extends this work to nonplanar faults, with a particular emphasis on understanding the connection between fault roughness and high-frequency ground motion.

## Data and Resources

The numerical simulations were conducted at the Stanford Center for Computational Earth and Environmental Science with computational support by Dennis Michael and Robert Clapp; at the Texas Advanced Computer Center (TACC) through a TeraGrid allocation; and on Harvard's BlueGene/L with support by Jayanta Sircar, Seppo Sahrakorpi, Suvendra Dutta, and the SEAS Cyberinfrastructure Lab.

## Acknowledgments

This work was initiated when E.M.D., D.B., and L.C. were at Harvard University. Work there was supported by the Southern California Earthquake Center (SCEC) as funded by Cooperative Agreements EAR-0529922 and USGS 07HQAG0008, the Harvard Faculty Aide program for undergraduate research (under the supervision of James R. Rice), matching funds from Harvard's Department of Earth and Planetary Sciences, and an award from the Highbridge Undergraduate Research Fund through Harvard's Department of Mathematics to D.B. Later work at Stanford by E.M.D. and J.E.K. was supported by NSF award EAR-0910574 and by SCEC (SCEC contribution number 1412). Discussions with James R. Rice, Elizabeth L. Templeton, and Robert C. Viesca throughout this project were invaluable. The insightful comments of Steven M. Day, David D. Oglesby, and an anonymous reviewer improved the manuscript.

## References


Andrews, D. J. (2005). Rupture dynamics with energy loss outside the slip zone, *J. Geophys. Res.* **110,** B01307, doi 10.1029/2004JB003191.

Ascher, U., and P. Lin (1997). Sequential regularization methods for nonlinear higher-index DAEs, *SIAM J. Sci. Comput.* **18,** no. 1, 160–181.

Beeler, N. M., and T. E. Tullis (1996). Self-healing pulse in dynamic rupture models due to velocity-dependent strength, *Bull. Seismol. Soc. Am.* **86,** 1130–1148.

Beeler, N. M., and T. E. Tullis (2003). Constitutive relationships for fault strength due to flash-heating, in *SCEC Annual Meeting Proceedings and Abstracts*, vol. XIII**,** 66, Southern California Earthquake Center, Los Angeles, California.

Beeler, N. M., T. E. Tullis, and D. L. Goldsby (2008). Constitutive relationships and physical basis of fault strength due to flash heating, *J. Geophys. Res.* **113,** B01401, doi 10.1029/2007JB004988.

Ben-Zion, Y., and Z. Shi (2005). Dynamic rupture on a material interface with spontaneous generation of plastic strain in the bulk, *Earth Planet Sci. Lett.* **236,** 486–496, doi 10.1016/j.epsl.2005.03.025.

Bhat, H. S., A. J. Rosakis, and C. G. Sammis (2010). An experimental and theoretical study of asymmetric earthquake rupture propagation caused by off-fault fracture damage, *American Geophysical Union Abstract T33B-2241, presented at 2010 Fall Meeting*, San Francisco, California, 13–17 December.

Brasey, V., and E. Hairer (1993). Half-explicit Runge–Kutta methods for differential-algebraic systems of index 2, *SIAM J. Num. Anal.*, **30,** no. 2, 538–552.

Brune, J. N., T. L. Henyey, and R. F. Roy (1969). Heat flow, stress, and rate of slip along the San Andreas fault, California, *J. Geophys. Res.* **74,** no. 15, 3821–3827.

Carpenter, M. H., and C. A. Kennedy (1996). Fourth-order 2N-storage Runge–Kutta schemes, *Tech. Rep. NASA TM-109112*, NASA Langley Research Center, Hampton, Virginia.

Carpenter, M. H., D. Gottlieb, and S. Abarbanel (1994). Time-stable boundary conditions for finite-difference schemes solving hyperbolic systems: Methodology and application to high-order compact schemes, *J. Comp. Phys.* **111,** no. 2, 220–236, doi 10.1006/jcph.1994.1057.

Cochard, A., and R. Madariaga (1994). Dynamic faulting under rate-dependent friction, *Pure Appl. Geophys.* **142,** 419–445.

Cochard, A., and R. Madariaga (1996). Complexity of seismicity due to highly rate-dependent friction, *J. Geophys. Res.* **101,** 25,321–25,336.

Di Toro, G., D. L. Goldsby, and T. E. Tullis (2004). Friction falls towards zero in quartz rock as slip velocity approaches seismic rates, *Nature* **427,** 436–439, doi 10.1038/nature02249.

Duan, B., and S. M. Day (2008). Inelastic strain distribution and seismic radiation from rupture of a fault kink, *J. Geophys. Res.* **113,** B12311, doi 10.1029/2008JB005847.

Dunham, E. M., D. Belanger, L. Cong, and J. E. Kozdon (2011). Earthquake ruptures with strongly rate-weakening friction and off-fault plasticity, Part 2: Nonplanar faults, *Bull. Seismol. Soc. Am.* **101,** no. 5, 2308–2322.

Gustafsson, B. (1981). The convergence rate for difference approximations to general mixed initial boundary value problems, *SIAM J. Num. Anal.* **18,** no. 2, 179–190.

Hairer, E., and G. Wanner (2004), *Solving Ordinary Differential Equations II: Stiff and Differential-Algebraic Problems*, Third ed., Springer, Berlin, Germany. 614 pp.

Hardebeck, J. L., and A. J. Michael (2004). Stress orientations at intermediate angles to the San Andreas Fault, California, *J. Geophys. Res.* **109,** B11303, doi 10.1029/2004JB003239.

Harris, R. A., M. Barall, R. Archuleta, E. Dunham, B. Aagard, J. P. Ampuero, H. Bhat, V. Cruz-Atienza, L. Dalguer, P. Dawson, S. Day, B. Duan, G. Ely, Y. Kaneko, Y. Kase, N. Lapusta, Y. Liu, S. Ma, D. Oglesby, K. Olsen, A. Pitarka, S. Song, and E. Templeton (2009). The SCEC/USGS dynamic earthquake rupture code verification exercise, *Seismol. Res. Lett.* **80,** no. 1, 119–126, doi 10.1785/gssrl.80.1.119.

Heaton, T. H. (1990). Evidence for and implications of self-healing pulses of slip in earthquake rupture, *Phys. Earth Planet. Inter.* **64,** 1–20.

Hickman, S., and M. Zoback (2004). Stress orientations and magnitudes in the SAFOD pilot hole, *Geophys. Res. Lett.* **31**, L15S12, doi 10.1029/2004GL020043.

Hirose, T., and T. Shimamoto (2005). Growth of a molten zone as a mechanism of slip weakening of simulated faults in gabbro during frictional melting, *J. Geophys. Res.* **110,** B05202, doi 10.1029/2004JB003207

Jaeger, J., N. Cook, and R. Zimmerman (2007). *Fundamentals of Rock Mechanics*, Fourth ed., Blackwell Publishing Ltd, Malden, Massachusetts.

Johnson, E. (1990). On the initiation of unilateral slip, *Geophys. J. Int.* **101,** 125–132.

Kennedy, C. A., and M. H. Carpenter (2003). Additive Runge–Kutta schemes for convection-diffusion-reaction equations, *Appl. Num. Math.* **44,** 139–181.

Kozdon, J. E., E. M. Dunham, and J. Nordström (2009). High-order treatment of fault boundary conditions using summation-by-parts finite difference methods, *Eos Trans. AGU* **90,** no. 52, Fall Meet. Suppl., Abstract S31A-1697.

Kozdon, J. E., E. M. Dunham, and J. Nordström (2011). Interaction of waves with frictional interfaces using summation-by-parts difference operators: Weak enforcement of nonlinear boundary conditions, *J. Sci. Comp.*, doi 10.1007/s10915-011-9485-3.

Kreiss, H.-O., and G. Scherer (1974). *Mathematical Aspects of Finite Elements in Partial Differential Equations*, edited by C. de Boor, Academic Press, New York, 195–212.

Kreiss, H.-O., and G. Scherer (1977). On the existence of energy estimates for difference approximations for hyperbolic systems, *Tech. Rep.*, Dept. of Scientific Computing, Uppsala University, Uppsala, Sweden.

Kreiss, H.-O., and G. Scherer (1992). Method of lines for hyperbolic differential equations, *SIAM J. Numer. Anal.* **29,** no. 3, 640–646.

Lachenbruch, A. H., and J. H. Sass (1980). Heat flow and energetics of the San Andreas fault zone, *J. Geophys. Res.* **85,** 6185–6223.

Lapusta, N., and J. R. Rice (2003). Low-heat and low-stress fault operation in earthquake models of statically strong but dynamically weak faults, *Eos Trans. AGU* **84,** no. 46, Fall Meet. Suppl., Abstract S51B-02.

Loret, B., and J. H. Prevost (1990). Dynamic strain localization in elasto-(visco-)plastic solids, Part 1. General formulation and one-dimensional examples, *Comput. Meth. Appl. Mech. Eng.* **83,** 247–273.

Lykotrafitis, G., A. J. Rosakis, and G. Ravichandran (2006). Self-healing pulse-like shear ruptures in the laboratory, *Science* **313,** no. 5794, 1765–1768, doi 10.1126/science.1128359.

Ma, S., and G. C. Beroza (2008). Rupture dynamics on a bimaterial interface for dipping faults, *Bull. Seismol. Soc. Am.* **98,** no. 4, 1642–1658, doi 10.1785/0120070201.

Mattsson, K., and J. Nordström (2004). Summation by parts operators for finite difference approximations of second derivatives, *J. Comp. Phys.* **199,** no. 2, 503–540, doi 10.1016/j.jcp.2004.03.001.

Mitchell, T. M., and D. R. Faulkner (2009). The nature and origin of off-fault damage surrounding strike-slip fault zones with a wide range of displacements: A field study from the Atacama fault system, northern Chile, *J. Struct. Geol.* **31,** 802–816, doi 10.1016/j.jsg.2009.05.002.

Noda, H., E. M. Dunham, and J. R. Rice (2009). Earthquake ruptures with thermal weakening and the operation of major faults at low overall stress levels, *J. Geophys. Res.* **114,** B07302, doi 10.1029/2008JB006143.

Palmer, A. C., and J. R. Rice (1973). The growth of slip surfaces in the progressive failure of over-consolidated clay, *Proc. R. Soc. London A* **332,** 527–548.

Perzyna, P. (1966). Fundamental problems in viscoplasticity, in *Advances in Applied Mechanics*, vol. **9,** edited by G. G. Chernyi, H. L. Dryden, P. Germain, L. Howarth, W. Olszak, W. Prager, R. F. Probstein, and H. Ziegler, pp. 243–377, Academic Press, New York, doi 10.1016/S0065-2156(08)70009-7.

Poliakov, A. N. B., R. Dmowska, and J. R. Rice (2002). Dynamic shear rupture interactions with fault bends and off-axis secondary faulting, *J. Geophys. Res.* **107,** doi 10.1029/2001JB000572.

Prakash, V., and F. Yuan (2004). Results of a pilot study to investigate the feasibility of using new experimental techniques to measure sliding resistance at seismic slip rates, *SCEC Ann. Prog. Rep.*, Southern California Earthquake Center.

Rice, J. R. (1983). Constitutive relations for fault slip and earthquake instabilities, *Pure Appl. Geophys.* **121,** no. 3, 443–475, doi 10.1007/BF02590151.

Rice, J. R. (1999). Flash heating at asperity contacts and rate-dependent friction, *Eos Trans. AGU* **80,** no. 46, Fall Meet. Suppl., F681.

Rice, J. R. (2006). Heating and weakening of faults during earthquake slip, *J. Geophys. Res.* **111,** no. B5, B05311, doi 10.1029/2005JB004006.

Rice, J. R., N. Lapusta, and K. Ranjith (2001). Rate and state dependent friction and the stability of sliding between elastically deformable solids, *J. Mech. Phys. Solids* **49,** 1865–1898.

Rice, J. R., C. G. Sammis, and R. Parsons (2005). Off-fault secondary failure induced by a dynamic slip-pulse, *Bull. Seismol. Soc. Am.* **95,** no. 1, 109–134, doi 10.1785/0120030166.

Rudnicki, J. W., and J. R. Rice (1975). Conditions for the localization of deformation in pressure-sensitive dilatant materials, *J. Mech. Phys. Solids* **23,** 371–394.

Saffer, D. M., B. A. Bekins, and S. Hickman (2003). Topographically driven groundwater flow and the San Andreas heat flow paradox revisited, *J. Geophys. Res.* **108,** no. B5, doi 10.1029/2002JB001849.

Sleep, N. H. (2010). Application of rate and state friction formalism and flash melting to thin permanent slip zones of major faults, *Geochem. Geophys. Geosyst.* **11,** Q05007, doi 10.1029/2009GC002997.

Sluys, L. J., and R. de Borst (1992). Wave propagation and localization in a rate-dependent cracked medium—Model formulation and one-dimensional examples, *Int. J. Solid Structures* **29,** no. 23, 2945–2958.

Strand, B. (1994). Summation by parts for finite difference approximations for $d/dx$, *J. Comp. Phys.* **110,** no. 1, 47–67, doi 10.1006/jcph.1994.1005.

Templeton, E. L., and J. R. Rice (2008). Off-fault plasticity and earthquake rupture dynamics: 1. Dry materials or neglect of fluid pressure changes, *J. Geophys. Res.* **113,** B09306, doi 10.1029/2007JB005529.

Tsutsumi, A., and T. Shimamoto (1997). High velocity frictional properties of gabbro, *Geophys. Res. Lett.* **24,** 699–702.

Tullis, T. E., and D. L. Goldsby (2003a). Flash melting of crustal rocks at almost seismic slip rates, *Eos Trans. AGU* **84,** no. 46, Fall Meet. Suppl., Abstract S51B-05.

Tullis, T. E., and D. L. Goldsby (2003b). Laboratory experiments on fault shear resistance relevant to coseismic earthquake slip, *SCEC Ann. Prog. Rep.*, Southern California Earthquake Center.

Viesca, R. C., E. L. Templeton, and J. R. Rice (2008). Off-fault plasticity and earthquake rupture dynamics: 2. Effects of fluid saturation, *J. Geophys. Res.* **113,** B09307, doi 10.1029/2007JB005530.

Williamson, J. H. (1980). Low-storage Runge–Kutta schemes, *J. Comp. Phys.* **35,** 48–56.

Zheng, G., and J. R. Rice (1998). Conditions under which velocity-weakening friction allows a self-healing versus a cracklike mode of rupture, *Bull. Seismol. Soc. Am.* **88,** 1466–1483.

Zoback, M. D., M. L. Zoback, V. S. Mount, J. Suppe, J. P. Eaton, J. H. Healy, D. Oppenheimer, P. Reasenberg, L. Jones, C. B. Raleigh, I. G. Wong, O. Scotti, and C. Wentworth (1987). New evidence for the state of stress on the San Andreas fault system, *Science* **238,** 1105–1111.

## Appendix

## Numerical Method

The governing equations, (1), (11), and (12), form a system of first-order partial differential equations with an algebraic constraint. For uniform material properties, they can be written as

$$\frac{\partial q}{\partial t} + \frac{\partial G_x(q)}{\partial x} + \frac{\partial G_y(q)}{\partial y} = \langle \lambda \rangle S(q), \tag{A1}$$

$$\eta \lambda = F(q). \tag{A2}$$

Here, $q$ is a vector containing velocities and stresses. The "fluxes" $G_i$ (so-called because $\partial G_x(q)/\partial x + \partial G_y(q)/\partial y$ is the divergence of the flux) are functions of material properties and $q$, and $\langle \lambda \rangle S(q)$ is a source term that is nonzero only during plastic flow.

The domain is discretized with a uniform mesh, and all components of velocity and stress are defined at each grid point (i.e., we do not use a staggered grid). Having all of the stress components at the same location greatly simplifies integration of the plasticity equations. The spatial derivatives are approximated using a summation-by-parts finite difference method (Kreiss and Scherer, 1974, 1977; Strand, 1994; Mattsson and Nordström, 2004); boundary conditions are enforced weakly using the simultaneous approximation term technique (Carpenter *et al.*, 1994). This method is provably stable, even with nonlinear rate-and-state friction laws, and the scheme is high-order accurate (Kozdon *et al.*, 2009). Specifically, the method is fifth-order accurate in the interior and third-order accurate near the boundaries; the entire scheme is globally fourth-order accurate (Gustafsson, 1981). A detailed description of the method for linear elasticity is given by Kozdon *et al.* (2011).

Timestepping equations (A1) and (A2) present a particular challenge due to the algebraic constraint. For simplicity of notation, we write these equations, after discretization of the spatial derivative terms and incorporation of the boundary conditions through penalty terms [both are combined into the single term $E(Q)$]:

$$\frac{dQ}{dt} + E(Q) = \langle \Lambda \rangle S(Q) \tag{A3}$$

and

$$\eta \Lambda = F(Q), \tag{A4}$$

where $Q$ is a vector containing the values of velocity and stress at all grid points and similarly for $\Lambda$. The equations are identified as a system of differential-algebraic equations (DAE). The particular form for rate-independent plasticity, which arises when $\eta = 0$, is that of an index 2 DAE (Hairer and Wanner, 2004). The choice of $\eta > 0$ can be viewed mathematically as a regularization procedure (Ascher and Lin, 1997) that reduces the index of the DAE to 1; this permits (A4) to be solved explicitly for the algebraic variable $\Lambda$. Substituting the result into (A3) yields the system of ordinary differential equations (ODE)

$$\frac{dQ}{dt} + E(Q) = \frac{\langle F(Q) \rangle}{\eta} S(Q). \tag{A5}$$

The $\eta \to 0$ limit is a singular one, and the ODE becomes increasingly stiff in this limit, necessitating the use of at least partially implicit timestepping methods. Such methods are, of course, required for the rate-independent equations; otherwise, the constraint equation could not be strictly enforced. However, it is highly desirable to explicitly evaluate the elastic term $E(Q)$, as this involves calculating spatial derivatives and would become prohibitively costly if done implicitly.

A variety of approaches can be used to solve equations (A3) and (A4). We focus entirely on one-step procedures, which update the fields from time $t^n$ to $t^{n+1} = t^n + \Delta t$, namely, from $Q^n$ to $Q^{n+1}$. The first, and perhaps simplest, method to do this is based on a first-order operator-splitting procedure. One first solves the elastic problem,

$$\frac{dQ}{dt} + E(Q) = 0, \tag{A6}$$

over the time interval $t^n$ to $t^{n+1}$ to update $Q^n$ to $Q^*$. An explicit timestepping method is most efficient; we use both third- and fourth-order low-storage Runge–Kutta methods (Williamson, 1980; Carpenter and Kennedy, 1996). Low-storage refers to the fact that only two storage units are required for each field; these are repeatedly overwritten at each internal Runge–Kutta stage. This substantially reduces memory requirements as compared with traditional Runge–Kutta methods.

We remark that it is necessary to use Runge–Kutta methods with at least three internal stages; this is the minimum that is required to have a stability region that contains the imaginary axis (e.g., Kreiss and Scherer, 1992). This is needed because several of the eigenvalues of the Jacobian of the ODE, $-\partial E/\partial Q$, are almost purely imaginary (as is typical for wave-propagation problems with minimal dissipation).

Next, using $Q^*$ as the initial condition on $Q$ at time $t^n$, one solves

$$\frac{dQ}{dt} = \langle \Lambda \rangle S(Q) \tag{A7}$$

and

$$\eta \Lambda = F(Q), \tag{A8}$$

over the time interval $t^n$ to $t^{n+1}$ to obtain $Q^{n+1}$. Note that this problem involves only fields defined at a particular grid point, which greatly simplifies the solution. The simplest numerical method to solve this problem is the first-order implicit Euler discretization:

$$\frac{Q^{n+1} - Q^*}{\Delta t} = \langle \Lambda^{n+1} \rangle S(Q^{n+1}) \tag{A9}$$

and

$$\eta \Lambda^{n+1} = F(Q^{n+1}), \tag{A10}$$

which requires the solution of these coupled nonlinear equations for $Q^{n+1}$ and $\Lambda^{n+1}$. For the Drucker–Prager model, this is readily done in closed form, permitting the efficient updating of the fields.

An alternative to the operator-splitting procedure that retains high-order accuracy during either elastic or plastic response (but has overall first-order accuracy due to the abrupt switching between elastic and plastic behavior), is to use coupled implicit-explicit (or additive) Runge–Kutta methods. For rate-independent plasticity, we found the third-order half-explicit Runge–Kutta method of Brasey and Hairer (1993), which is designed specifically for index 2 DAEs, to be highly efficient. We have also successfully used several of the high-order methods proposed by Kennedy and Carpenter (2003). None of these methods are written in a low-storage form and hence increase memory requirements.

For the grid spacings used in this study, the predominant source of error comes from approximating the spatial derivatives of fields in the term $E(Q)$; it makes little difference which time-integration method we use. Hence, we default to the simplest operator-splitting method in this work, but we do note that on certain test problems at high resolution, the coupled implicit-explicit methods give superior performance.

Department of Geophysics
Stanford University
397 Panama Mall
Stanford, California 94305
edunham@stanford.edu
jkozdon@stanford.edu
(E.M.D., J.E.K.)

BBN Technologies
10 Moulton Street
Cambridge, Massachusetts 02138
dbelange@bbn.com
(D.B.)

Stanford Graduate School of Business
518 Memorial Way
Stanford, California 94305
wtsung@stanford.edu
(L.C.)

Manuscript received 24 March 2010